



Phase transition and possible metallization in CeVO_4 under pressure



Alka B. Garg^{a,*}, K.V. Shanavas^{a,1}, B.N. Wani^b, Surinder M. Sharma^a

^a High Pressure and Synchrotron Radiation Physics Division, Bhabha Atomic Research Centre, Mumbai 400085, Maharashtra, India

^b Chemistry Division, Bhabha Atomic Research Centre, Mumbai 400085, Maharashtra, India

ARTICLE INFO

Article history:

Received 18 December 2012

Received in revised form

19 April 2013

Accepted 22 April 2013

Available online 4 May 2013

Keywords:

High pressure

X-ray diffraction

Phase transition

CeVO_4

First principles calculations

Electrical resistance

ABSTRACT

Phase stability of CeVO_4 under pressure has been investigated using synchrotron based angle dispersive x-ray diffraction (ADXRD), electrical resistance and first principles calculations. The results indicate that the ambient zircon structure of the compound transforms to a low symmetry monoclinic monazite phase beyond 3.8 GPa with nearly 8.6% volume discontinuity. Beyond 11 GPa, the pattern could be fitted to a similar monazite structure which is about 12.7% denser and has a much larger monoclinic beta angle. On pressure release the first monoclinic phase is recovered. The electrical resistance data show a large drop in resistance with pressure indicating substantial narrowing down of the band gap. Electronic structure calculations support these observations and suggest possible pressure induced metallization in this material.

© 2013 Elsevier Inc. All rights reserved.

1. Introduction

Rare earth *ortho*-vanadates ($\text{R}^{3+}\text{V}^{5+}\text{O}_4^{2-}$; where *R* is the rare earth element including Y and Sc) is a subset of family of RBO_4 type compounds (where *B* is a penta-valent cation) which are being studied as potential candidates for many existing and future technologies. For example, rare earth *ortho*-phosphates (RPO_4) and rare earth *ortho*-arsenates (RASO_4) are being used as chemically durable nuclear waste matrices [1–3]. Rare earth *ortho*-vanadates (RVO_4) and *ortho*-phosphates have recently emerged as promising materials for solid-state lasers (Nd:YVO₄ most important diode-pumped solid-state laser) [4–6], thermophosphors [7] and γ ray scintillators [8,9] which has led the researchers to investigate the various optical, electronic [10–15], magnetic [16–18], elastic [19,20], structural [21,22] and other properties of this class of materials by various experimental and computational means. The physical properties of solids are sensitive to its crystal structure and ionic radii play an important role in determining the crystal structures. The most common structure adopted by RBO_4 type of compounds at ambient pressure and temperature are zircon, scheelite and monazite. The RPO_4 and RASO_4 , compounds with larger rare earth cations adopt the monazite structure whereas the compounds with smaller rare

earth cations tend to adopt the zircon structure. Most of the rare earth *ortho*-vanadates crystallize in the zircon structure. However, the LaVO_4 (largest rare earth cation) can also be stabilized in monoclinic monazite structure (bimorphic) at ambient pressure and temperature conditions depending on the method of synthesis [23,24]. As has been stated earlier the optical properties of these compounds have been studied extensively but their mechanical and electrical properties are far less known. It is well known that pressure is one thermodynamic variable which can be used to tune the crystal structure and in turn the mechanical properties of the materials.

Recently high pressure investigations on a variety of zircon structured (space group $I4_1/amd$) compounds which include rare earth *ortho*-vanadates and rare earth *ortho*-phosphates have established that generally these compounds transform to another low symmetry quenchable tetragonal scheelite (space group $I4_1/a$) phase under moderate pressure (≤ 10 GPa) [25–35]. This scheelite phase is nearly 10% denser than the zircon phase due to the efficient packing of the polyhedra. The zircon-to-scheelite transition has also been investigated from the point of view of the mechanism and kinetics of the transition [36–38]. Many of the larger rare earth cations based *ortho*-phosphates transform to monoclinic monazite ($P2_1/n$) phase under pressure [39,40]. The basic units of zircon structured compounds are chain of alternating $\text{V}(\text{P})\text{O}_4$ and RO_8 polyhedra extending parallel to the *c* axis. The chains are joined laterally by edge-sharing RO_8 dodecahedra. Due to the technological importance of RVO_4 compounds, there have been focused efforts to study the phase stability of these materials

* Corresponding author. Fax: +91 22 25505296.

E-mail addresses: alkagarg@barc.gov.in, garalka@gmail.com (A.B. Garg).

¹ Present address: Department of Physics & Astronomy, University of Missouri, Columbia, MO 65211.

under various thermodynamic conditions. Results of x-ray diffraction and Raman spectroscopic measurements under compression show zircon to scheelite and then to fergusonite phase transition in LuVO_4 [29,30], YbVO_4 [28], EuVO_4 [33]. The high pressure x-ray diffraction investigations on ScVO_4 [33] and YVO_4 [31] do not show scheelite to fergusonite phase transition upto 27 GPa and 26 GPa respectively. However, more recent Raman studies and ab-initio calculations carried out on these compounds under high pressure do show the scheelite to fergusonite phase transition in YVO_4 beyond 20 GPa [34] and ScVO_4 beyond 18.2 GPa [35]. It is interesting to note that depending on the technique used for identifying the pressure induced phase transition, the transition pressure may vary based on local or non local character of the technique [41]. In all these studies the scheelite phase is retained on pressure release.

The fact that LaVO_4 can be stabilized in zircon/monoclinic phase at ambient pressure and temperature conditions, it is expected that the rare earth based zircon compounds with relatively larger ionic radii should follow a different phase transition sequence. CeVO_4 (Ce^{3+} is the second largest ion next to La^{3+} in the lanthanide series) lies at the zircon monazite phase boundary indicating that this compound should transform at low pressure. Apart from the physics point of view, due to unique optical, electrical and redox properties, CeVO_4 is of considerable interest for counter electrodes in electro-chromic devices. Hence it further enhances the importance to study their mechanical and electrical behavior against pressure.

The first report of high pressure experimental work by Stubican and Roy [42] on CeVO_4 did not show any structural phase transition up to 8 GPa. Osamu Fukunaga and Shinobu Yamaoka [43] observed the phase transformation at low pressure of about 1 GPa and 600 °C. This transition is accompanied by a volume decrease of 8%. These researchers also predicted that it may transform to the scheelite form under higher pressure. Recent high pressure x-ray diffraction measurements on CeVO_4 have shown that this material transforms to a monoclinic monazite phase beyond 4 GPa [44,45]. Our high pressure Raman measurements showed that the material transforms from zircon to low symmetry phase near 4 GPa. Beyond 13 GPa intensity of Raman modes decreases considerably indicating another phase transition in the compound [46].

In the present work we have re-visited the high pressure behavior of CeVO_4 through x-ray diffraction, electrical resistance and first principles calculations.

2. Experimental and computational details

2.1. Sample preparation

A stoichiometric amount of CeO_2 (Alfa 99.99%) and V_2O_5 (Aldrich 99.6%) such that $\text{Ce}:\text{V}=1:1$ was taken for preparing CeVO_4 . The reactants (~1 g) were ground with an agate mortar and pestle for 30 min. Pellets were made and heated to 600 °C at a rate of ~5 °C/min and held for 6 h at 600 °C. The temperature was then raised to 800 °C at a rate of 10 °C/min and held for another 6 h and then cooled to room temperature. The sample was reground and re-pelletized and final sintering was carried out at 900 °C for 24 h. Although cerium ions in the starting oxide were not trivalent, the CeVO_4 compound was confirmed to be formed after sintering.

2.2. X-ray diffraction measurements

In-situ high pressure x-ray diffraction measurements were carried out at the XRD1 beamline of Elettra synchrotron source, Italy.

The data were collected in angle dispersive x-ray diffraction (ADXRD) mode, in the transmission geometry. The wavelength of the x-ray employed and the sample to image plate (IP) distance were calibrated using CeO_2 diffraction pattern. Hardened stainless steel gasket with a central hole of diameter 150 μm indented to a thickness of 50 μm contained the sample. For high pressure measurements, fine powdered CeVO_4 along with platinum as internal pressure calibrant and methanol–ethanol (4:1) mixture as pressure transmitting medium were loaded in a Mao–Bell-type diamond anvil cell (DAC) with diamond anvils of culet size 400 μm . X-ray powder patterns at various pressures were collected employing x-ray of wavelength 0.652 Å collimated to 80 μm diameter. Typical exposure times of 15–20 min were employed for measurements at high pressures. Images of the powder diffraction rings were read from the MAR345 image plate area detector with a pixel size of $100 \times 100 \mu\text{m}^2$. The images thus obtained were integrated using the program FIT2D [47].

2.3. Electrical resistance measurements

For electrical resistance measurements under high pressure a clamp type Merrill Bessett DAC with a diamond culet size of 400 μm was used. Mylar embedded alumina coated on stainless steel gasket is used as sample chamber. Two stainless steel wires of 20 μm diameter with separation of 30 μm or less are used as leads for quasi-four probe measurements. Pressure is measured by monitoring the shift in ruby fluorescence lines [48]. A small rectangular piece of the sample prepared by pressing the powdered sample between the two diamonds of another DAC is kept at the center of the anvil face touching both wires. Constant current is passed through the two leads and voltage is measured across the sample. Initially when the resistance of the sample is very high ($\text{G}\Omega$) two probes are used for resistance measurements however when the resistance is in the $\text{M}\Omega$ range four probe measurements are carried out with a constant current of 100 μA . The details of the technique are reported elsewhere [49].

2.4. First principles calculations

Electronic structure calculations were carried out using VASP (Vienna simulation package) code (see Refs. [50,51] and references therein) with generalized gradient approximation [52–54] and projected augmented-wave [55] method to approximate the core electrons, while explicitly treating 12 valence electrons for Ce ($4f^1 5s^2 5p^6 5d^1 6s^2$), 11 for V ($3p^6 3d^4 4s^1$) and 6 for O ($2s^2 2p^4$). As was shown that inclusion of on-site coulomb interaction with Hubbard U applied to the f states of Ce is necessary to generate the correct insulating ground state of CeVO_4 , we used the approach described by Dudarev et al. [56] within GGA+U with a U–J of 4.5 eV. A kinetic energy cutoff of 500 eV and Monkhorst Pack k-point grid of $6 \times 6 \times 6$ was found sufficient to ensure convergence. The lattice constants and fractional coordinates for the zircon and monoclinic phases determined from experiments were used as the starting structures for the simulations.

Complete ionic relaxation was carried out on zircon and monoclinic structures at various volumes in ferromagnetic spin arrangement to find the lowest energy configurations. For this, symmetry and volume of the simulation box was fixed and the ionic degrees of freedom were allowed to relax till the Hellmann–Feynmann forces are less than 10^{-3} eV/Å. To determine the relative stability of the monoclinic phase compared to the zircon phase these calculations were repeated at different volumes.

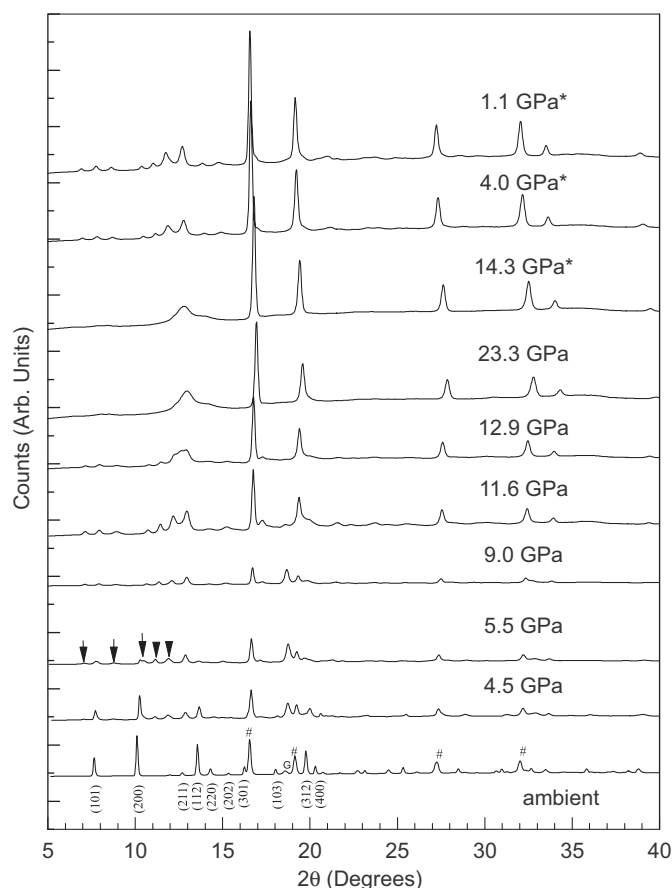


Fig. 1. Pressure evolution of x-ray diffraction patterns of CeVO_4 . The asterisks denote the data during pressure unloading. The ambient structure zircon peaks from the sample has been indexed. The reflection from the gasket has been marked as G and # denotes the peaks from the pressure calibrant. Arrows indicate the appearance of new diffraction peaks from the sample.

3. Results and discussion

Fig. 1 shows the evolution of the x-ray diffraction (XRD) patterns for CeVO_4 as a function of pressure. Up to 3.8 GPa, the diffraction patterns could be indexed to the ambient tetragonal zircon structure (space group $I4_1/amd$). The XRD pattern collected at 4.4 GPa showed new diffraction peaks. As the pressure was further increased, the intensity of new diffraction peaks increased, while the peaks corresponding to the zircon phase became weaker. The d values of the new peaks could be fitted to a monoclinic monazite structure (space group $P2_1/n$) as reported earlier [44,45]. On further increasing the pressure to 7.6 GPa, the peaks from zircon phase decreased below the detectable limit implying almost full transformation to the monazite phase. The co-existence of the two phases was observed over a pressure region from 4.4 GPa to 6.8 GPa which is quite small compared to the pressure range of co-existence during zircon to scheelite phase transition in similar compounds. There is no noticeable change in the diffraction patterns on further increasing the pressure except the shift of the peaks to higher angle with pressure. However, the pattern at 12.8 GPa shows considerable broadening of the diffraction profiles of CeVO_4 though the peaks from the platinum pressure calibrant remain sharp. This is the same pressure region where our earlier reported Raman data showed the loss of intensity of Raman peaks suggesting another phase transition [46]. Similar intensity loss of Raman peaks has been reported in Ref. [45] in the same pressure region. This pattern could be fitted to another monazite phase, differing from the earlier one in terms of a much larger monoclinic β angle (implying a large distortion of earlier monoclinic phase). Hereafter we call this phase as monazite II. The monazite I to monazite II transition has also been reported earlier in CePO_4 and PbCrO_4 [57–58]. This transition in PbCrO_4 is accompanied by band gap collapse. The lattice parameters obtained for the second high pressure phase were obtained using Rietveld refined lattice parameters of just preceding data as initial estimate. In Table 1, Rietveld refined structural parameters for all

Table 1

The structural parameters of the various phases of CeVO_4 as obtained from the Rietveld refinements of the experimental data.

(a) Structural parameters of CeVO_4 in ambient zircon phase (tetragonal symmetry, space group $I4_1/amd$, $Z=4$) at 0.5 GPa

$a=b=7.3998(4)$ Å, $c=6.4959(5)$ Å, $\alpha=\beta=\gamma=90^\circ$, $V=355.70(4)$ Å³

$W_{\text{RP}}=7.7\%$, $R_p=5.35\%$, $R(F^2)=19.62\%$

Atom	x	y	z
Ce	0.000000	0.750000	0.125000
V	0.000000	0.250000	0.375000
O	0.000000	0.4622(18)	0.2044(21)

(b) Structural parameters of CeVO_4 in monazite I phase at 10.7 GPa (monoclinic symmetry, space group $P2_1/n$, $Z=4$)

$a=6.7847(26)$ Å, $b=6.9780(24)$ Å, $c=6.5518(20)$ Å, $\alpha=\gamma=90^\circ$, $\beta=104.72(4)^\circ$

$V=300.01(19)$ Å³

$W_{\text{RP}}=5.2\%$, $R_p=3.56\%$, $R(F^2)=12.52\%$

Atom	x	y	z
Ce	0.288699	0.152499	0.120927
V	0.310867	0.172339	0.638123
O1	0.240387	−0.020244	0.464984
O2	0.436280	0.323755	0.539834
O3	0.534730	0.077485	0.811189
O4	0.138907	0.231941	0.709652

(c) Structural parameters of CeVO_4 in monazite II phase at 15.8 GPa (monoclinic symmetry, space group $P2_1/n$, $Z=4$)

$a=6.459(20)$ Å, $b=6.777(14)$ Å, $c=6.479(18)$ Å, $\alpha=\gamma=90^\circ$, $\beta=115.26(15)^\circ$

$V=256.5(12)$ Å³

$W_{\text{RP}}=3.56\%$, $R_p=2.27\%$, $R(F^2)=13.67\%$

Atom	x	y	z
Ce	0.206154	0.111233	0.846864
V	0.249281	0.151372	0.414735
O1	0.088902	0.587245	0.300050
O2	0.160395	0.280049	0.544032
O3	0.681954	0.351385	0.755270
O4	0.024163	0.079115	0.784040

three phases is given along with various residuals. The low value of residuals ($W_{RP}=3.56\%$, $R_p=2.27\%$, $R(F^2)=13.67\%$) for the second high pressure phase should imply good confidence in identifying the structure as monazite II. All the patterns beyond 11.1 GPa could be fitted to this structure. However, in principle, one cannot rule out the possibility that structure of second high pressure phase may depend upon the degree of nonhydrostatic stresses, which may help rationalize the claim of observing an orthorhombic phase (by Le-Bail fitting) in Ref. [44]. It is well known that once methanol–ethanol freezes into a soft solid beyond 10 GPa, the pressure conditions in diamond anvil cell are quasihydrostatic. So the diffraction data collected in the present work with methanol–ethanol pressure transmitting medium will have larger deviatoric stresses [59–61] than the one reported in Ref. [44] with neon as pressure transmitting medium. Here it is worth commenting few more observation about the effect of various pressure transmitting mediums giving different nonhydrostaticity to the sample. The first high pressure phase transition from zircon to monazite is observed at almost same pressure irrespective of the pressure

medium implying similar hydrostatic environment to the sample. However on pressure increase beyond 10 GPa, the nonhydrostatic component is more in the case of methanol–ethanol than neon hence the observed transition pressure for the second high pressure phase is lower with methanol–ethanol pressure transmitting medium than neon. A few diffraction patterns were also collected during pressure unloading. On pressure release the monazite I phase was recovered.

Multi-phase Rietveld refinement of all the patterns were carried out to extract information on structural evolution using the versatile and most widely used GSAS software [62]. In all the patterns, diffraction peaks from the platinum pressure marker have also been refined to extract the pressure experienced by the sample using equation of state (pressure volume data at ambient temperature) of platinum [63]. Fig. 2 shows the multi-phase Rietveld refined patterns of the ambient zircon, monazite I, monazite II and pressure released monazite I phase. Fig. 3 depicts cell parameters for all the three phases along with earlier data with neon as pressure transmitting medium [44]. In the zircon

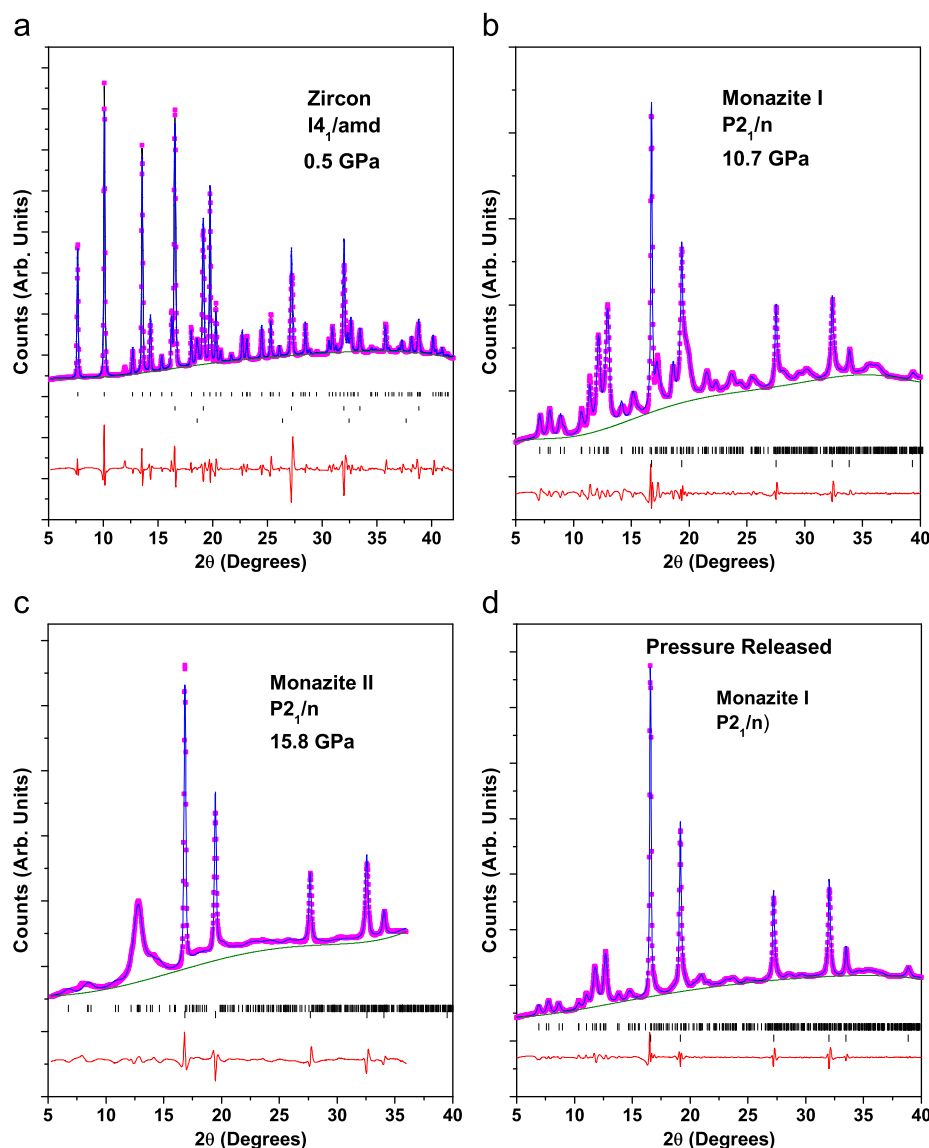


Fig. 2. Rietveld refined diffraction patterns: (a) ambient zircon phase, (b) monazite I phase, (c) monazite II phase, (d) monazite I phase recovered upon pressure release. Symbols denote the experimental data points and line denoted the calculated profile. Background and difference plots have also been plotted. In (a) upper vertical tick marks are for zircon phase, middle vertical marks are for the pressure calibrant. In (b)–(d), the upper tick marks represent monazite I, monazite II and recovered monazite I phases, respectively, while the pressure calibrant is represented by lower tick marks. (For interpretation of the references to color in this figure legend, the reader is referred to the web version of this article.)

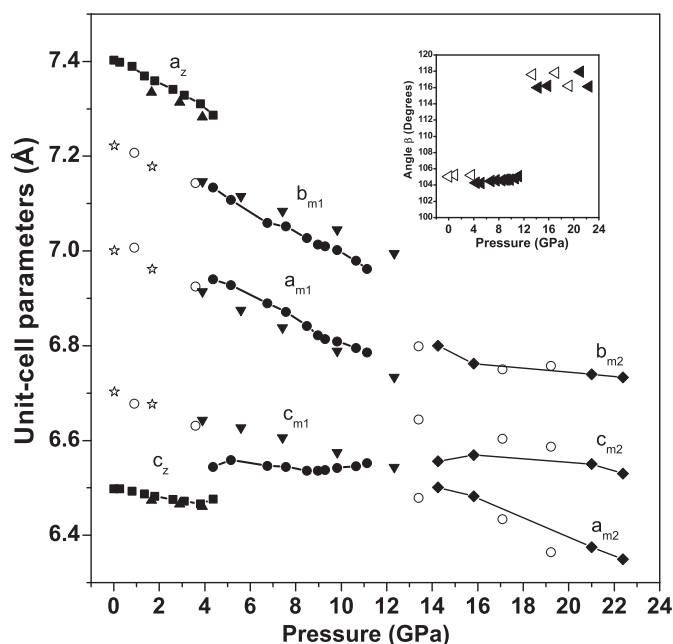


Fig. 3. Pressure evolutions of the unit-cell parameters for the three phases of CeVO_4 . Inset shows the variation of monoclinic β angle (Filled [\blacktriangle] are during pressure loading and open [\triangleleft] are the data points during pressure unloading). Note the sudden change in the β angle from monazite I to monazite II transition. The filled squares [\blacksquare] represent the data for ambient zircon phase obtained in present studies whereas the filled up triangle [\blacktriangle] is from Ref. [44] for the same phase. The filled circles [\bullet] denote the data for monoclinic I phase obtained in present studies whereas the filled down triangle triangles [\blacktriangledown] is from Ref. [44] for the same phase. The solid diamond [\blacklozenge] depicts the data for monazite II phase. Open circles [\circ] are for the data during pressure unloading from the present studies whereas open star [\star] is the data from Ref. [44] during pressure releasing cycle.

phase, the a axis is more compressible than the c axis indicating nonisotropic compression of the unit cell, an effect observed due to differential bond compressibility [64,65]. Similar behavior is reported in other rare earth *ortho*-vanadates also. In the case of monazite I phase, the a and b axis decreased with pressure whereas the c axis remains almost constant, our this observation of nonisotropic compression in monazite phase for CeVO_4 is similar to the one observed in other ABO_4 compounds adopting the monazite structure [64]. The pressure (P) versus volume (V) data for all three phases (zircon, monazite I and monazite II) is shown in Fig. 4. The zircon to monazite I transition is accompanied by a large change in the volume (8.6%). During transition from monazite I to monazite II, monoclinic β angle increases which is shown as the inset in Fig. 4. The volume change during monazite I to monazite II is 12.7%.

The bulk modulus of zircon phase of CeVO_4 is obtained by fitting the experimental pressure volume data to the 2nd-order Birch–Murnaghan (B–M) equation of state [66]. The fitted value of ambient pressure volume (V_0) and bulk modulus (B_0) comes out to be 356.53 \AA^3 (very close to the published value 355.82 \AA^3 [67]) and $112(3) \text{ GPa}$ respectively with pressure derivative of bulk modulus B'_0 fixed at 4. This value of bulk modulus is quite close to the value of 119 GPa reported earlier with methanol–ethanol pressure medium [45] and little lower than the value of 125 GPa with neon as pressure medium [44]. The experimental pressure volume data in the monazite I phase when fitted to the 2nd-order B–M equation of state gives the B_0 to be $98(3) \text{ GPa}$ with $V_0 = 328.23 \text{ \AA}^3$ (again very close to the published value of 329.02 \AA^3 [68]). The reason for observing lower value of bulk modulus in high pressure phase is discussed in the later section.

Fig. 5(a) shows the total energy E as a function of volume (per formula unit of CeVO_4) in the zircon and monoclinic phases.

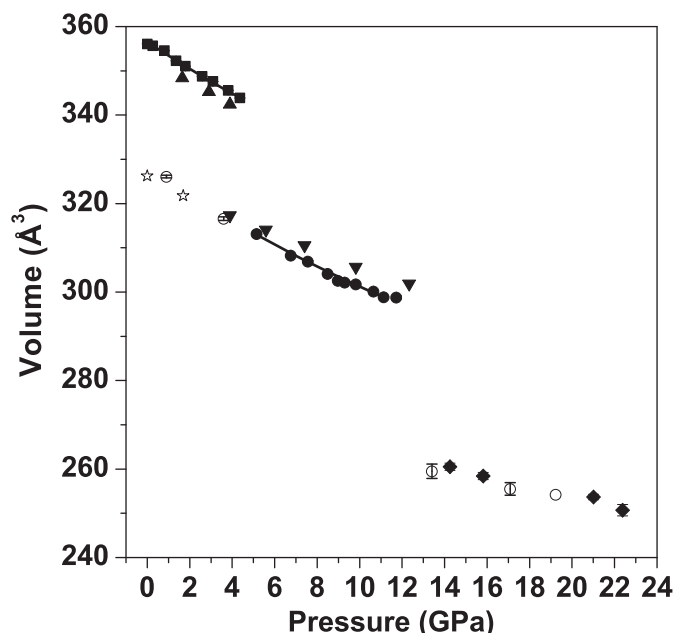


Fig. 4. Pressure–volume data for the ambient and high pressure phases of the CeVO_4 . The filled squares [\blacksquare] represent the data for ambient zircon phase obtained in present studies whereas the filled up triangle [\blacktriangle] is from Ref. [44] for the same phase. The filled circles [\bullet] denote the data for monoclinic I phase obtained in present studies whereas the filled down triangle triangles [\blacktriangledown] is from Ref. [44] for the same phase. The solid diamond [\blacklozenge] depicts the data for monazite II phase. Open circles [\circ] indicate the data during pressure unloading from the present studies whereas open star [\star] is the data from Ref. [44] during pressure releasing cycle. Error bars in the volume have also been plotted. The solid line is the second order B–M equation of fit to the observed data for ambient zircon and monazite I phase.

Enthalpy difference between the monoclinic phases and the zircon phase as a function of pressure are plotted in Fig. 5(b). The solid lines in Fig. 5(a) are fits of the computed data of parent and daughter phases to the B–M equation of state. From the fit, we find the bulk modulus for zircon phase to be 125 GPa , which is exactly matching with the previously reported data obtained with neon as pressure medium [44] and close to earlier published value of 120 GPa through computation [45] and our experimental value of 112 GPa . For the first high pressure monoclinic phase, the computed bulk modulus of 100 GPa is also close to 109 GPa reported in previous computations [45] and almost perfectly matches with our experimental value of 98 GPa . For 2nd high pressure monoclinic phase the computed bulk modulus was determined to be 238 GPa . The experimental bulk modulus for the second monazite phase was estimated as 189 GPa . We would like to emphasize here that, since determination of bulk modulus using B–M equation of state requires extrapolation of volume data to ambient pressures, the errors in zero pressure volumes (since the second monazite phase is reversible, the data have to be necessarily be extrapolated to obtain V_0 , ambient pressure volume) may lead to large errors in the bulk modulus. Another reason for differences could be the limited number of data points (both experimental and theoretical).

Fig. 5(a) shows that below 82 \AA^3 monazite I is of lower energy state. Upon further reduction in volume, monazite II phase is found to be more stable implying monazite I to monazite II transition. Plot of enthalpy differences between zircon and monoclinic phases as a function of pressure shown in Fig. 5(b) confirm the two successive phase transitions to monazite I at $\sim 9 \text{ GPa}$ and monazite II at $\sim 20 \text{ GPa}$, respectively. Considering the inherent approximations in DFT, the present values of transition pressures are in good agreement with the experimentally observed transition pressures.

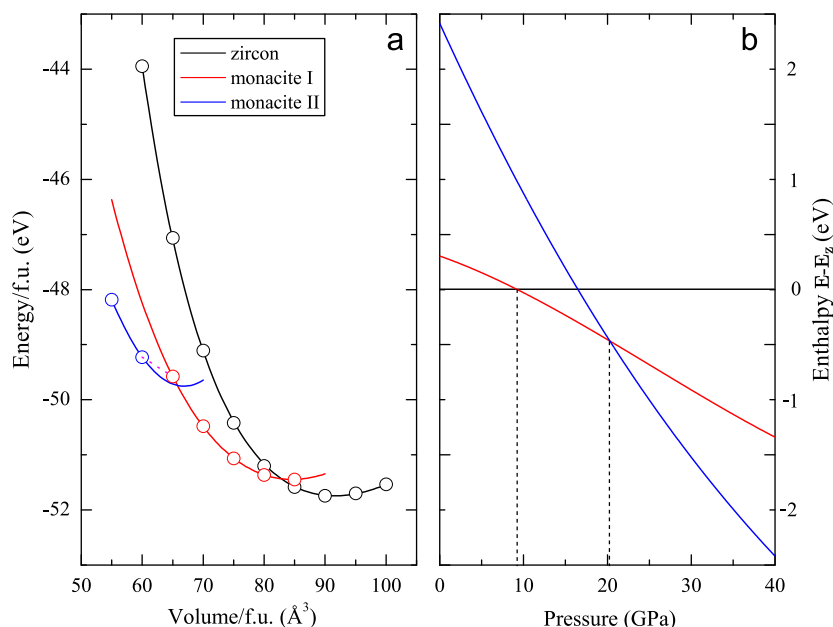


Fig. 5. Calculated equation of state of CeVO_4 from first principles. (a) Energy per functional unit as a function of volume/f.u. of the unit cell; (b) Enthalpy difference between the monoclinic phases and the zircon phase as a function of pressure. Vertical lines indicate pressures of phase transitions. (For interpretation of the references to color in this figure legend, the reader is referred to the web version of this article.)

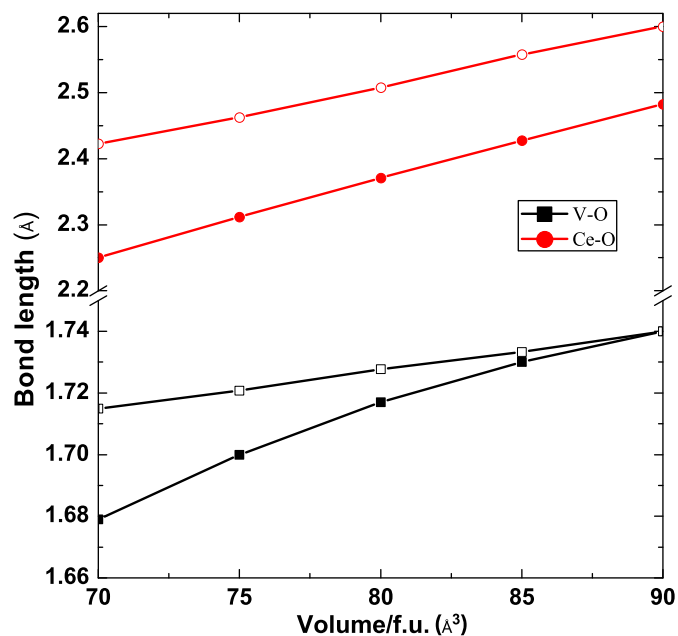


Fig. 6. Calculated variations of average V–O and Ce–O bond lengths under compression. Closed symbols represent zircon and open symbols represent monacite I phase.

The lower bulk modulus observed in experiments and calculations for the monacite I phase can be understood in terms of the cation–ligand bond lengths shown in Fig. 6. Due to higher symmetry, the distortions and rotations of the VO_4 tetrahedra in zircon phase are restricted under compression whereas in the monacite phase lower symmetry may permit distortions and as a consequence it can utilize the free volume in the structure. As can be seen from Fig. 6, this leads to lower Ce–O and V–O bond lengths in the zircon phase compared to the monacite phase at the same volume. The reduction in V–O bond lengths are also higher in the zircon phase under compression resulting in larger energy cost for compression (refer to Fig. 5(a)) and in turn higher bulk

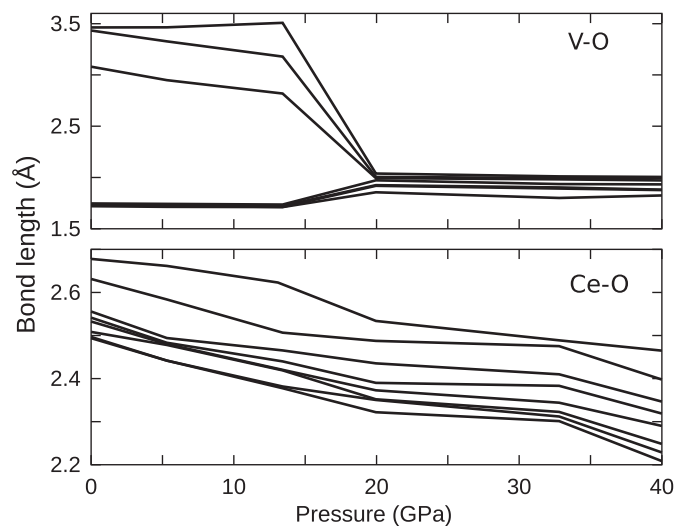


Fig. 7. Calculated nearest neighbor Ce–O and V–O distances in monacite I and monacite II phases of CeVO_4 as a function of pressure.

modulus. Our calculations suggest that monacite I–II transition is accompanied by an increase in coordination of V ions as can be seen from Fig. 7. The four coordinated vanadium ions become seven coordinated in the second monoclinic phase. The coordination of Ce ions remains more or less unchanged. As width of the bond lengths in the figure suggests that the distribution of oxygen around V ions is more ordered than around Ce probably as a consequence of the f orbital participating in the bonding.

In Fig. 8, we show the electrical resistance variation of CeVO_4 under pressure. The starting value of the resistance is in $\text{G}\Omega$ region indicating the insulating behavior of the material (CeVO_4 is the direct band gap insulator at ambient pressure and temperature with a band gap of 1.8 eV measured by diffused reflectance spectroscopy [69]). As the pressure is slowly increased the resistance of the sample decreased indicating the continuous narrowing down of the band gap. However at around 12 GPa the resistance value decreases by more than an order of magnitude indicating

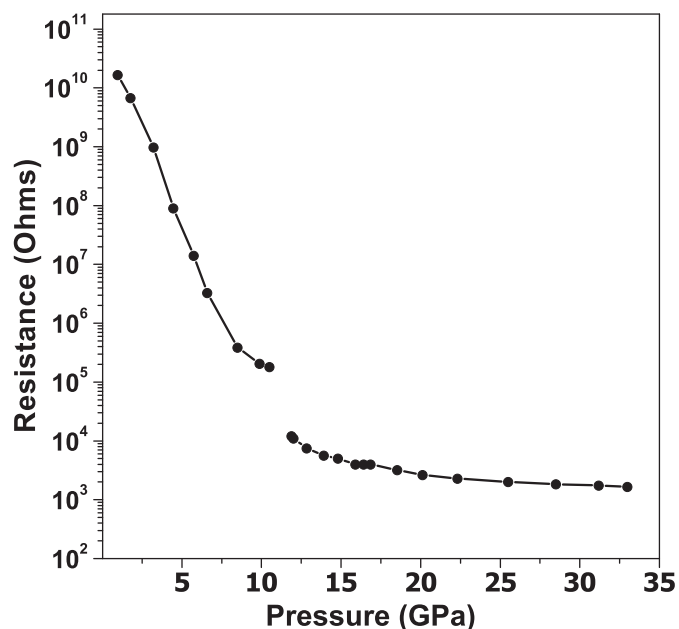


Fig. 8. Observed variation of electrical resistance of CeVO_4 with pressure.

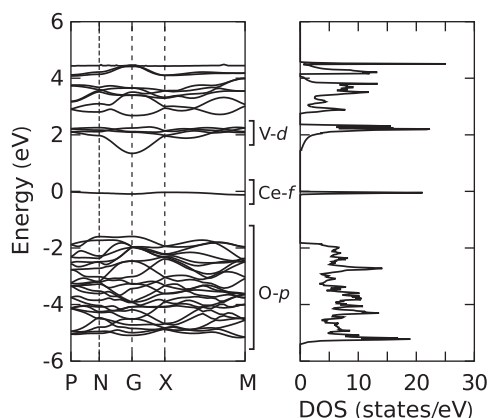


Fig. 9. Spin polarized band structure of CeVO_4 in the zircon phase at ambient pressure along high symmetry lines for the antiferromagnetic structure. The Fermi level is at 0 eV.

sudden changes in the material. This is the same pressure region where monazite I to monazite II transition is observed. On further increasing the pressure up to 33 GPa (the highest pressure reached in the present investigations) the resistance value continued to decrease but with slower rate.

To understand this from a theoretical point of view, we calculated the band structure of zircon and monoclinic structures at different pressures. The ambient pressure band structure for the zircon phase in the AFM spin arrangement is shown in Fig. 9. As we can see, the narrow Ce- f states lie between the occupied oxygen- p states and empty V- d states. The band gap measured from the top of Ce- f and V- d is about 1.6 eV, which is slightly lower than the experimentally reported value of 1.8 eV by diffused reflectance spectroscopy. The variation of electronic structure under pressure across the monazite-I to II transition can be seen from the density of states (DOS) shown in Fig. 10. The DOS plots in the monazite-I (at 0 and 18 GPa) and monazite-II (at 55 GPa) phases of CeVO_4 show that band gap reduces and eventually closes under pressure. At low pressures [Figs. 9 and 10(a)], as expected

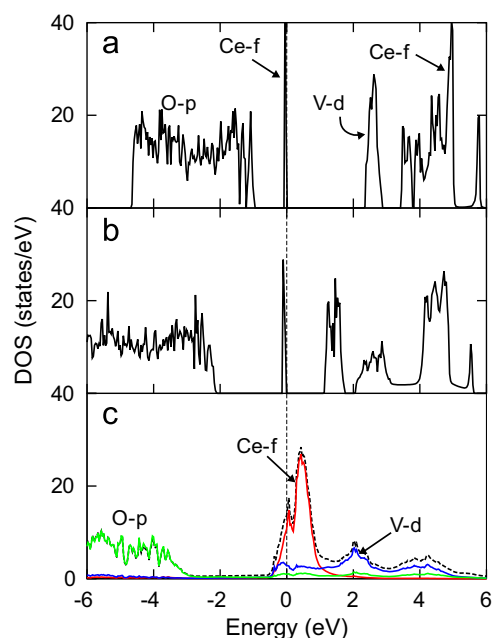


Fig. 10. Density of states at different volumes/f.u. in the monoclinic phases for the spin up channel. In (a) 85 Å^3 (0 GPa) and (b) 70 Å^3 (18 GPa) the structure is first monazite phase while (c) 55 Å^3 (55 GPa) is in the second monazite phase. Fermi level is set to 0 eV. In the insulating phase the valence band is a narrow Ce- f band and conduction band is V- d band. When compressed, the band gap reduces and eventually merges leading to a metallic phase.

from the ionic charge model, the oxygen p -states are full (O^{2-}), the vanadium d - and s -states are empty (V^{5+}) and Ce has one electron in f -states with empty s -states (Ce^{3+}). The valence band top (HOMO) is made up of Ce- f band to which each Ce ion contributes one electron. This band is very narrow with a band width of ~ 0.1 eV as expected from highly localized f -electrons. The conduction band is predominantly V- d states and the rest of Ce- f states lie above this band due to strong Coulomb repulsion within the f -band. The system is insulating at low pressures, but upon compression the reduction of Ce–O and V–O bond lengths pushes the V- d band closer to the Fermi level and leads to reduction in band gap. At 70 Å^3 the band gap has reduced to ~ 1.1 eV as can be seen from Fig. 10 (b). Eventually, at very high pressures at 55 GPa, the gap has completely vanished suggesting that the system has become metallic. This is consistent with our experimental observations.

To conclude, the phase stability of CeVO_4 under pressure has been investigated using in-situ x-ray diffraction, electrical resistance and first principles calculations. The ambient phase of the compound is stable upto 3.8 GPa. Beyond this pressure the material shows a first-order structural transition to a low symmetry monoclinic phase with a large volume discontinuity. Co-existence of two phases was also observed over a small pressure region. On further increasing the pressure, beyond 11 GPa there is another phase transition to similar monazite phase with large distortion and increase in monoclinic β angle. The electrical resistance data along with first-principles calculations indicate metallization in this material. The experimental bulk modulus for the zircon and high pressure monoclinic phases matches reasonably well with the theoretically calculated results. On pressure release the less distorted monoclinic phase is recovered.

Acknowledgment

Alka B. Garg gratefully acknowledges the financial support through India–Italy POC for experiments at Elettra synchrotron.

References

- [1] L.A. Boatner, G.W. Beall, M.M. Abraham, C.B. Finch, R.J. Floran, P.G. Huray, M. Rappaz, Management of Alpha-Contaminated Wastes, IAEA-SM-246/73, IAEA, Vienna, 1981, p. 411.
- [2] L.A. Boatner, M.M. Abraham, B.C. Sales, Inorg. Chim. Acta 94 (1984) 146–148.
- [3] L.A. Boatner, G.W. Beall, M.M. Abraham, C.B. Finch, P.G. Huray, M. Rappaz, in: C. J. Northrup (Ed.), Scientific Basis for Nuclear Waste Management, Plenum, New York, 1980, p. 289.
- [4] K. Byrappa, B. Nirmala, K.M. Lokanatha Rai, M. Yoshimura, in: Kullaiah Byrappa, Tadashi Ohachi, Walter Michaeli, Hans Warlimont, Eicke Weber (Eds.), Crystal Growth Technology, William Andrew Inc., 2003, pp. 335–364.
- [5] A. Rapaport, V. David, M. Bass, C. Dekka, L.A. Boatner, J. Lumin. 85 (1999) 155–161.
- [6] Alexandra Rapaport, Olivier Moteau, Michael Bass, L.A. Boatner, Chiranjit Dekka, J. Opt. Soc. Am. B16 (1999) 911–916.
- [7] S.W. Allison, L.A. Boatner, G.T. Gillies, Appl. Opt. 34 (1995) 5624–5627.
- [8] A. Lempicki, E. Berman, A.J. Wojtowicz, M. Balcerzyk, L.A. Boatner, IEEE Trans. Nucl. Sci. 40 (1993) 384–387.
- [9] A.J. Wojtowicz, D. Wisniewski, A. Lempicki, L.A. Boatner, in: J.P. Biersack (Ed.), Radiation Effects and Defects in Solids, 135, Overseas Publishers Association, Amsterdam, 1995, p. 305.
- [10] N.I. Lazukova, V.A. Gubanov, M.P. Butsman, V.M. Cherkashenko, A.A. Fotiev, J. Struct. Chem. 21 (1980) 286–290.
- [11] F.W. Kutzler, D.E. Ellis, D.J. Lam, B.W. Veal, A.P. Paulikas, A.T. Aldred, V.A. Gubanov, Phys. Rev. B29 (1984) 1008–1021.
- [12] V.A. Gubanov, D.E. Ellis, A.A. Fotiev, J. Solid State Chem. 21 (1977) 303–324.
- [13] M. Moussa, M. Djermouni, S. Kacimi, M. Azzouz, A. Dahani, A. Zaoui, Comput. Mater. Sci. 68 (2013) 361–366.
- [14] V. Panchal, D. Errandonea, A. Segura, P. Rodriguez-Hernandez, A. Munoz, S. Lopez-Moreno, M. Bettinelli, J. Appl. Phys. 110 (2011) 043723–043733.
- [15] M.R. Dolgos, A.M. Paraskos, M.W. Stoltzfus, S.C. Yarnell, P.M. Woodward, J. Solid State Chem. 182 (2009) 1964–1971.
- [16] Y. Hirano, S. Skanthakumar, C.-K. Loong, N. Wakabayashi, L.A. Boatner, Phys. Rev. B66 (2002) 024424–024430.
- [17] S. Skanthakumar, C.-K. Loong, L. Soderholm, M.M. Abraham, L.A. Boatner, Phys. Rev. B51 (1995) 12451–12457.
- [18] M.-D. Guo, A.T. Aldred, S.-K. Chan, J. Phys. Chem. Solids 48 (1987) 229–235.
- [19] J. Nipko, M. Grimsditch, C.-K. Loong, S. Kern, M.M. Abraham, L.A. Boatner, Phys. Rev. B53 (1996) 2286–2290.
- [20] Yukiko Hirano, Ilde Guedes, Marcus Grimsditch, Chun-Keung Loong, Nobuyoshi Wakabayashi, Lynn A. Boatner, J. Am. Ceram. Soc. 85 (2002) 1001–1003.
- [21] Yoshio Oka, Takeshi Yao, Naichi Yamamoto, J. Solid State Chem. 152 (2000) 486–491.
- [22] H. Fuess, A. Kallel, J. Solid, State Chem. 5 (1972) 11–14.
- [23] U. Kolitsch, D. Holtstam, Eur. J. Miner. 16 (2004) 117–126.
- [24] C.E. Rice, W.R. Robinson, Acta Cryst B32 (1976) 2232–2233.
- [25] Daniel Errandonea, Francisco Javier Manjón, Prog. Mater. Sci. 53 (2008) 711–773.
- [26] A. Tatsi, E. Stavrou, Y.C. Boulmetis, A.G. Kontos, Y.S. Raptis, C. Raptis, J. Phys.: Condens. Matter 20 (2008) 425216–425222.
- [27] F.X. Zhang, M. Lang, R.C. Ewing, J. Lian, Z.W. Wang, J. Hu, L.A. Boatner, J. Solid State Chem. 181 (2008) 2633–2638.
- [28] Alka B. Garg, Rekha Rao, T. Sakuntala, B.N. Wani, V. Vijayakumar, J. Appl. Phys. 106 (2009) 063513–063518.
- [29] R. Mittal, Alka B. Garg, V. Vijayakumar, S.N. Achary, A.K. Tyagi, B.K. Godwal, E. Busetto, A. Lausiand, S.L. Chaplot, J. Phys.: Condens. Matter 20 (2008) 075223–075229.
- [30] Rekha Rao, Alka B. Garg, T. Sakuntala, S.N. Achary, A.K. Tyagi, J. Solid State Chem. 182 (2009) 1879–1883.
- [31] X. Wang, I. Loa, K. Syassen, M. Hanfland, B. Ferrand, Phys. Rev. B70 (2004) 064109–064114.
- [32] F.X. Zhang, J.W. Wang, M. Lang, J.M. Zhang, R.C. Ewing, Phys. Rev. B80 (2009) 184114–184120.
- [33] D. Errandonea, R. Lacombe-Perales, J. Ruiz-Fuertes, A. Segura, S.N. Achary, A.K. Tyagi, Phys. Rev. B79 (2009) 184104–184112.
- [34] F.J. Manjón, P. Rodríguez-Hernández, A. Muñoz, A.H. Romero, D. Errandonea, K. Syassen, Phys. Rev. B81 (2010) 075202–075212.
- [35] V. Panchal, F.J. Manjón, D. Errandonea, P. Rodriguez-Hernandez, J. L'opez-Solano, A. Mu-noz, S.N. Achary, A.K. Tyagi, Phys. Rev. B83 (2011) 064111–064120.
- [36] M. Marques, J. Contreras-Garcia, M. Florez, J.M. Recio, J. Phys. Chem. Solids 69 (2009) 2277–2280.
- [37] M.B. Smirnov, A.P. Mirgorodsky, V.Yu. Kazimirov, R. Guinebretière, Phys. Rev. B78 (2008) 094109–094119.
- [38] A.K. Mishra, Nandini Garg, K.K. Pandey, K.V. Shanavas, A.K. Tyagi, Surinder M. Sharma, Phys. Rev. B81 (2010) 104109–104114.
- [39] R. Lacombe-Perales, D. Errandonea, Y. Meng, M. Bettinelli, Phys. Rev. B81 (2010) 064113–064121.
- [40] E. Stavrou, A. Tatsi, E. Salpea, Y.C. Boulmetis, A.G. Kontos, Y.S. Raptis, C. Raptis, J. Phys.: Conf. Ser. 121 (2008) 042016–042021.
- [41] Francisco Javier Manjón, Daniel Errandonea, Phys. Status Solidi B 246 (2009) 9–31.
- [42] V.S. Stubican, R. Roy, Z. Kristallogr. Miner. 119 (1963) 90–97.
- [43] Osamu Fukunaga, Shinobu Yamaoka, Phys. Chem. Miner. 5 (1979) 167–177.
- [44] D. Errandonea, R.S. Kumar, S.N. Achary, A.K. Tyagi, Phys. Rev. B84 (2011) 224121–224128.
- [45] V. Panchal, S. López-Moreno, D. Santamaría-Pérez, D. Errandonea, F.J. Manjón, P. Rodríguez-Hernandez, A. Muñoz, S.N. Achary, A.K. Tyagi, Phys. Rev. B84 (2011) 024111–024122.
- [46] Rekha Rao, Alka B. Garg, B.N. Wani, J. Phys.: Conf. Ser. 377 (2012) 012010–012013.
- [47] A.P. Hammersley, S.O. Svensson, M. Hanfland, A.N. Fitch, D. Hausermann, High Press. Res. 14 (1996) 235–248.
- [48] H.K. Mao, J. Xu, P.M. Bell, J. Geophys. Res. 91 (1986) 4673–4676.
- [49] A.B. Garg, V. Vijayakumar, B.K. Godwal, Rev. Sci. Instrum. 75 (2004) 2475–2478.
- [50] G. Kresse, J. Hafner, Phys. Rev. B47 (1993) 558–561.
- [51] G. Kresse, J. Furthmüller, Phys. Rev. B54 (1996) 11169–11186.
- [52] J.P. Perdew, K. Burke, Y. Wang, Phys. Rev. B54 (1996) 16533–16539.
- [53] J.P. Perdew, K. Burke, M. Ernzerhof, Phys. Rev. Lett. 77 (1996) 3865–3868.
- [54] G. Kresse, D. Joubert, Phys. Rev. B59 (1999) 1758–1775.
- [55] E. Blöchl, Phys. Rev. B50 (1994) 17953–17979.
- [56] S.L. Dudarev, G.A. Botton, S.Y. Savrasov, C.J. Humphreys, A.P. Sutton, Phys. Rev. B57 (1998) 1505–1509.
- [57] Tony Huang, Jiann-Shing Lee, Jennifer Kung, Chih-Ming Lin, Solid State Commun. 150 (2010) 1845–1850.
- [58] E. Bandiello, D. Errandonea, D. Martinez-Garcia, D. Santamaria-Perez, F.J. Manjón, Phys. Rev. B85 (2012) 024108–024117.
- [59] S. Klotz, J.C. Chervin, P. Munsch, G. Le Marchand, J. Phys. D: Appl. Phys. 42 (2009) 075413–075419.
- [60] D. Errandonea, Y. Meng, M. Somayazulu, D. Hausermann, Physica, B355, 116–125.
- [61] S.M. Sharma, Y.M. Gupta, Phys. Rev. B58 (1998) 5964–5971.
- [62] A.C. Larson, R.B. Von Dreele, GSAS: General Structure Analysis System Los Alamos National Laboratory Report No. LAUR, 2000, pp. 86–748.
- [63] J.C. Jamieson, J.N. Fritz, M.H. Manghnani, in: S. Akimoto, M.H. Manghnani (Eds.), High Pressure Research in Geophysics, Reidel, Boston, 1982, pp. 27–48.
- [64] R. Lacombe-Perales, D. Errandonea, Y. Meng, M. Bettinelli, Phys. Rev. B81 (2010) 064113–064121.
- [65] A.K. Mishra, Nandini Garg, K.V. Shanavas, S.N. Achary, A.K. Tyagi, Surinder M. Sharma, J. App. Phys. 110 (2011) 123505–123510.
- [66] F. Birch, J. Geophys. Res. 83 (1978) 1257–1268.
- [67] Bryan C. Chakoumakos, Marvin M. Abraham, Lynn A. Boatner, J. Solid State Chem. 109 (1994) 197–202.
- [68] M. Yoshimura, T. Sata, Bull. Chem. Soc. Jpn. 42 (1969) 3195–3198.
- [69] M.R. Dolgos, A.M. Paraskos, M.W. Stoltzfus, S.C. Yarnell, P.M. Woodward, J. Solid State Chem. 182 (2009) 1964–1971.